

Article

Particle Swarm Optimization-Based Power and Temperature Control Scheme for Grid-Connected DFIG-Based Dish-Stirling Solar-Thermal System

Yang Li ¹, Binyu Xiong ^{1,*}, Yixin Su ¹, Jinrui Tang ¹ and Zhiwen Leng ²

¹ Department of Electrical Engineering, School of Automation, Wuhan University of Technology, Wuhan 430070, Hubei, China; y.li@msn.com (Y.L.); suyixin@whut.edu.cn (Y.S.); tangjinrui@whut.edu.cn (J.T.)

² China Ship Development and Design Center, Wuhan 430064, Hubei, China; coldwing@sina.com

* Correspondence: bxiong2@whut.edu.cn; Tel.: +86-136-5710-7813

Received: 6 February 2019; Accepted: 29 March 2019; Published: 4 April 2019



Abstract: Variable-speed operation of a dish-Stirling (DS) concentrated solar-thermal power generating system can achieve higher energy conversion efficiency compared to the conventional fixed-speed operation system. However, tuning of the controllers for the existing control schemes is cumbersome due to the presence of a large number of control parameters. This paper proposes a new control system design approach for the doubly-fed induction generator (DFIG)-based DS system to achieve maximum power point tracking and constant receiver temperature regulation. Based on a developed thermo-electro-pneumatic model, a coordinated torque and mean pressure control scheme is proposed. Through steady-state analysis, the optimal torque is calculated using the measured insolation and it serves as the tracking reference for direct torque control of the DFIG. To minimize the tracking error due to temperature variation and the compressor loss of the hydrogen supply system, four optimal control parameters are determined using particle swarm optimization (PSO). Model-order reduction and the process of the pre-examination of system stability are incorporated into the PSO algorithm, and it effectively reduces the search effort for the best solution to achieve maximum power point tracking and maintain the temperature around the set-point. The results from computational simulations are presented to show the efficacy of the proposed scheme in supplying the grid system with smoothed maximum power generation as the solar irradiance varies.

Keywords: concentrated solar-thermal power generation; dish-Stirling (DS) system; doubly-fed induction generator (DFIG); particle swarm optimization (PSO); maximum power point tracking (MPPT)

1. Introduction

Modern electricity supply systems have experienced significant changes due to the rapid increase of renewable energy generation in the past decades. Amongst various renewable energy technologies, dish-Stirling (DS) concentrated solar-thermal power generating system uses a parabolic dish-like reflector to collect and concentrate sunlight to a small heat receiver located at the focal point of the reflector. The high temperature achieved at the focal point, in which the receiver is located, is used as a heat source for a closed-cycle external heat engine called Stirling engine [1]. The DS system is capable of operating at a high energy conversion efficiency and releases no emissions, and thus it is considered to be a promising sustainable technology for future power grid structures such as microgrid and distributed generation [2].

For these reasons, in recent years, grid-connected DS system has received the attention of researchers aiming toward improving its modelling, design, control, and simulation, in order to

increase the energy conversion efficiency and lower the overall cost of the system. A mathematical model intended for the optimal opto-geometric design of the concentrator and heat receiver is proposed in [3] and it is experimentally verified in [4]. Thermal efficiency of the heat receiver is studied and validated in [5]. A thermal model of a cavity receiver is developed for optimization in [6] where radiative exchange is evaluated using the radiosity method. The authors in [7] show that the global energy efficiency ranges between 19% and 26%, which can be achieved through optimal design based on a modified Iwamoto model of a Stirling engine and a solar prediction model. Further increase of utilization and efficiency can be achieved by incorporating novel components such as a free-piston Stirling engine [8], high-temperature superconducting linear synchronous generator [9], or integrated thermal energy storage [10]. These works mainly focus on the optimization and design for a specific component. System-level modelling, control, and simulation have been studied in References [11,12], where an ideal adiabatic model of a double-acting kinematic Stirling engine was used. In order to achieve acceptable accuracy, this Stirling engine model requires a very small step size (about 2 μ s) for time-domain simulation as it has to be solved numerically as a cyclic boundary problem [13]. Due to the high complexity of the model, the control system can only be designed using empirical methods. A simple controller with proportional gain has to be used for the receiver temperature control, which causes lower thermal efficiency during the low insolation period. In [14], an averaged-value model of a solar Stirling engine is developed for the purpose of grid-integration studies and model-based control system design. The required step size for simulation is greatly increased to be compatible with that of electromechanical transient simulation. The control system has been improved with reduced impact on the interconnected grid system during insolation variation and/or grid fault. However, the scale of the conventional grid-connected DS system using squirrel-cage induction generators (SCIGs) is restricted due to the lack of control capability to meet the grid code requirements such as to provide frequency and voltage support. Although frequency support, such as a fixed-speed generation system, could be achieved by changing the working temperature [15], the significant reactive power injected to the grid system can still cause a severe voltage stability problem especially in a weak grid, as has been investigated in works [16,17].

In contrast, a variable-speed DS system is equipped with a doubly-fed induction generator (DFIG) [18,19] or permanent magnet synchronous generator (PMSG) [20,21]. With the back-to-back ac/dc/ac converters and advanced control techniques, independent regulation of the active power and reactive power becomes feasible. Maximum power point tracking (MPPT) and ancillary services, such as the frequency and voltage regulation, can be achieved for additional technological and economic benefits. Compared to PMSG, DFIG is more attractive as it is cheaper than PMSG and its power converter devices have a lower power rating. In [18], the authors propose two effective MPPT schemes by using direct power control, and perturbation and observation method, but the behaviors and limitations of thermodynamics and heat transfer of the prime mover have not been considered. In [19], it is found that the detailed modelling of the prime mover is important for a DS system as the control strategy of the prime mover can affect system stability when it is connected to the utility grid. However, the analysis and control system design presented is based on a simplified electrical model of DFIG, power converter, and grid system. In order to reduce the negative impact of temperature variation, a Takagi-Sugeno fuzzy supervisor is designed for several local state-feedback temperature controller to handle the nonlinearity of the system. As the control system is complex, the tuning of control parameters is cumbersome and no detailed discussion has been given.

To this end, in order to achieve the variable-speed operation of DS system with reduced effort in the control system design, this paper develops a new coordinated torque and mean pressure control scheme as well as a control parameter tuning method for MPPT and constant temperature regulation. The contribution of the work includes three aspects. First, a multi-physics dynamic model for a DFIG-based DS system has been established. For the first time, the detailed pneumatic model of the hydrogen supply system has been incorporated with the capability to consider the loss due to a gas compressor and limitation of external tanks. Second, a control scheme for a DFIG-based DS system

is proposed to achieve simultaneous maximum power point tracking and temperature regulation with less complexity. Through steady-state analysis of the developed model, the optimal torque to for maximum power harnessing is calculated from the measured insolation, and then implemented using direct torque control, while a simple PI controller is used for temperature regulation. Third, to minimize the tracking error due to the disturbance of the temperature variation and the consumed power by the compressor, the optimal control parameters are determined using particle swarm optimization (PSO). With the incorporation of model order reduction and pre-examination of the system stability, the search effort can be greatly reduced.

The rest of the paper is organized as follows. Section 2 presents the overall system configuration and the modeling of the grid-connected DFIG-based DS system. Section 3 develops the control scheme with a simple control structure using direct torque control for active power regulation and using mean pressure control for temperature regulation. Section 4 proposes a method to use PSO to obtain the optimal control parameters with the consideration of system stability. Numerical examples are included in Section 5 to show the validity of the developed model and the effectiveness of the proposed control system. Section 6 concludes the main findings of the work.

2. Modeling of a DFIG-Based DS System

2.1. System Configuration

The energy conversion of a typical DS system consists of three processes: First, the parabolic dish collects, reflects, and concentrates the direct normal irradiance of the sunlight into a small hollow chamber called the receiver. Second, a Stirling engine converts the high temperature heat accumulated in the receiver into mechanical energy. Finally, an electrical generator, driven by the Stirling engine, converts mechanical energy into electricity. Figure 1 shows the schematic of the DS system as well as the power and mass flows between/with the sub-systems.

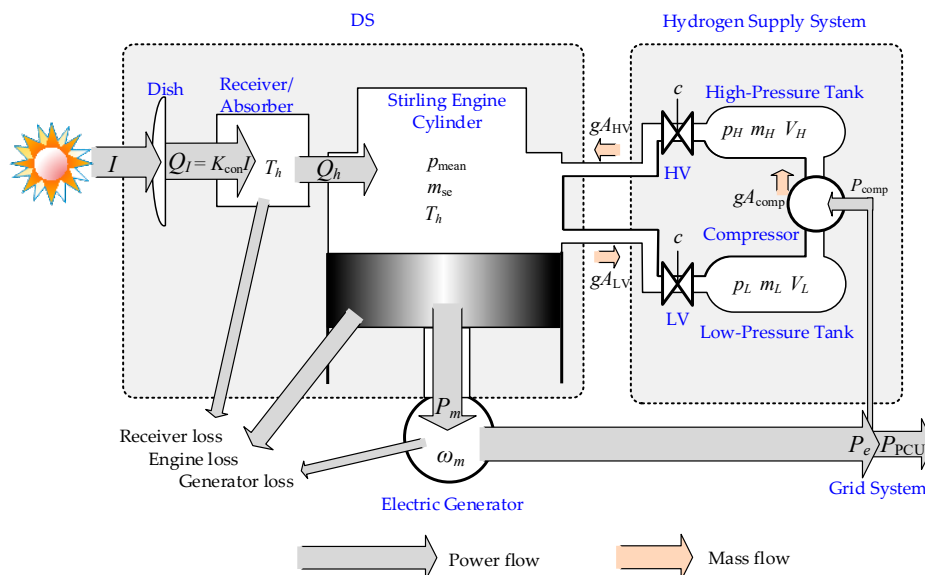


Figure 1. Schematic of dish/receiver-absorber, average-value single-cylinder equivalence to a double-acting kinematic Stirling engine, electric generator, and hydrogen supply system.

In contrast to the use of a fixed-speed SCIG in a conventional DS system [1], the variable-speed DFIG-based DS system studied in References [18,19] incorporates a wound-rotor induction generator and a back-to-back ac/dc/ac converter to interconnect the rotor windings of the generator to the grid. Although with similar structure to commercially-available DFIG-based wind turbine generator (WTG), the power rating of the prime mover of DS system, i.e., the Stirling engine, is much lower than that of a wind turbine. Many such generating units would have to be aggregated in some suitable

manner to realize a utility-scale power station. Figure 2 shows the schematic of a possible configuration of such a power generating station. It is based on the use of a multi-string-converter, consisting of a common dc-link and a common grid-side converter (GSC) similar to that described in [22] for a photovoltaic plant.

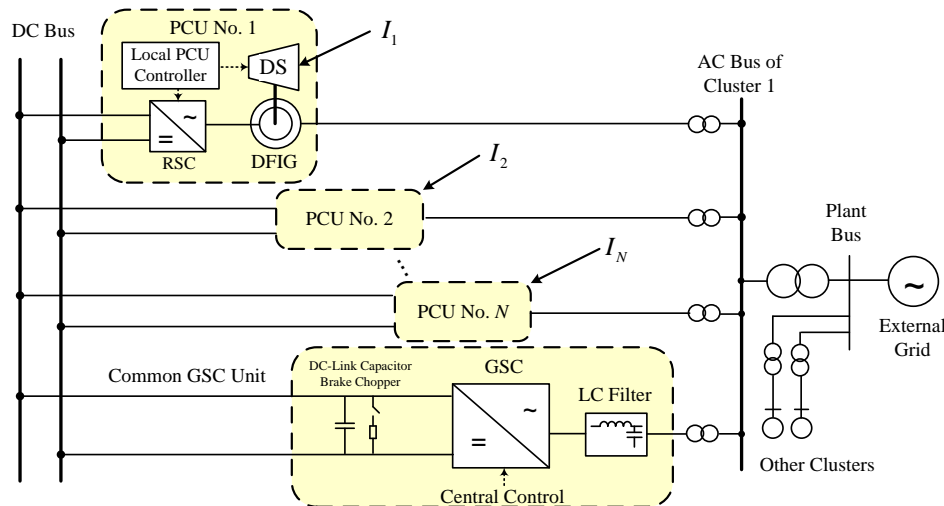


Figure 2. Proposed configuration of a DFIG-based DS solar-thermal power plant using a common dc bus and a common GSC unit.

In Figure 2, the DFIG-based DS power plant is shown to consist of a number of clusters in which each cluster consists of N power conversion units (PCU) and one common GSC unit. Each PCU contains a prime mover (the DS), a DFIG, a rotor-side converter (RSC), and a corresponding local control system. The dc terminals of RSCs from the N PCUs are connected to a common dc bus. The common GSC unit consists of a three-phase voltage source inverter, dc-link capacitor, the associated line filter, and a GSC controller. Similar to the observations made in [22], there are several distinct advantages in the proposed configuration. First, power flows can still be controlled through the individual PCU. However, as a GSC with a larger power-rating tends to have a lower specific cost ($\$/\text{kW}$) than that of a lower-rating GSC in this power level, the multi-string-converter configuration is therefore economically attractive. Moreover, a smoothing effect due to the expected diversity of the insolation level (I_k) among the PCU in a cluster would yield smaller power variations on the common dc bus. This would facilitate the control of the common GSC. Enhanced functionality of GSC, such as with regard to power quality and reactive power control, can also be achieved more economically using the larger-capacity converter.

Thus, with the configuration shown in Figure 2, each RSC is to achieve active power control of its PCU and to provide reactive power to the external grid. As long as the dc-link voltage is effectively maintained by the common GSC, the RSC can be individually controlled. The main drawback of the common GSC is that should it malfunction, the dc-link voltage may increase to some unacceptable level as the cluster is unable to export power to the grid. If this occurs, a braking resistor in the common brake chopper circuit in Figure 2 is inserted to dissipate the surplus energy and maintain the dc voltage. Other possible solution includes the use of an AC crowbar to short-circuit the rotor windings, and the DFIG then operates as a SCIG. However, such a contingency condition is not discussed in this article as this is considered a rare occurrence.

This work mainly studies the modeling and the local control of the PCU. The modeling of the power converters, dc bus, and grid system can be found in various literature such as [23].

2.2. Prime Mover Model

The prime mover of the PCU consists of the concentrator (i.e., the dish), the heat receiver/absorber, and the Stirling engine. It is shown as “DS” in Figures 1 and 2. The dish and the receiver are modelled using a normalized heat transfer equation [24]:

$$T_{\text{rec}} \frac{dT_h}{dt} = K_{\text{rec}}(K_{\text{con}}I - Q_h) - (T_h - T_a) \quad (1)$$

where I is the insolation level, T_a is the ambient temperature, Q_h is the rate of the heat flow absorbed by the Stirling engine, and the receiver temperature is assumed to be the same as the absorber/heater temperature T_h of the Stirling engine. Constants T_{rec} , K_{rec} , and K_{con} are as defined in [24], and their parametric values are determined according to the thermal characteristics of the receiver/absorber materials.

For the study of the variable-speed operation of the DS system, the behaviors of a double-acting kinematic Stirling engine with four series-connected cylinders can be described by an average-value adiabatic model with single-cylinder equivalence and the correction of losses:

$$Q_h = a_{00} + a_{10}p_{\text{mean}} + a_{01}\omega_m + a_{11}p_{\text{mean}}\omega_m + A(gA_{\text{se}}) + Cp_{\text{mean}} \frac{dT_h}{dt} \quad (2)$$

$$P_m = \tau_m\omega_m = b_{00} + b_{10}p_{\text{mean}} + b_{01}\omega_m + b_{11}p_{\text{mean}}\omega_m + b_{02}\omega_m^2 + b_{12}p_{\text{mean}}\omega_m^2 \quad (3)$$

$$p_{\text{mean}} = K_p m_{\text{se}} \quad (4)$$

where P_m , τ_m , and ω_m are mechanical power, mechanical torque, and rotating angular speed of the Stirling engine, respectively. p_{mean} and m_{se} are the average mean pressure and the total mass of the hydrogen in the engine cylinder, respectively. p_{mean} is proportional to m_{se} , and the gain K_p is a constant. gA_{se} is the mass flow rate of the hydrogen from engine cylinder to hydrogen tanks. The constants a_{00} , a_{01} , a_{10} , a_{11} , b_{00} , b_{01} , b_{10} , b_{11} , b_{02} , and b_{12} are multivariable coefficients to represent the steady-state performance of the Stirling engine. Constants A and C are also defined in [24], and their parametric values are governed by the dimension and performance characteristics of the Stirling engine. These parameters shall also be affected by the working temperature T_h . However, as T_h is assumed to be well maintained at a maximum value $T_{h,\text{max}}$, the effect of temperature variation on these parameters is ignored. Note that all the parameters and variables given in Equations (1)–(4) are expressed in per unit, and the base values are selected and given in Table 1. The per unit parameters of the prime mover model used in this work are given in Table 2.

Table 1. Per unit system for the prime mover and hydrogen supply system quantities.

Quantity	Description	Symbol	Base Value
Insolation	Maximum insolation	I_N	1000 W/m ²
Power	Nominal engine power	$P_{m,N}$	27 kW
Pressure	Max. mean pressure in the cylinder	p_N	20 MPa
Temperature	Max. heater/receiver temperature	T_N	1033 K
Speed	Nominal engine speed	$\omega_{m,N}$	190.63 rad/s
Mass	Max. hydrogen mass in the cylinder	m_N	0.0036 kg
Volume	$(m_N/M)RT_N/p_N$	V_N	7.667×10^{-4} m ³
Torque	$P_{m,N}/\omega_{m,N}$	τ_N	141.63 N

Table 2. Prime mover model and hydrogen supply system model parameters.

Param.	Value	Param.	Value	Param.	Value
K_{con}	2.865	b_{01}	0.055	n_c	1.027
K_{rec}	1.756	b_{11}	1.21	η_{comp}	0.7
T_{rec}	13.436 s	b_{02}	−0.026	T_k, T_{comp}	0.313
T_a	0.288	b_{12}	−0.13	$T_{h,\text{max}}$	1
a_{00}	0.045	A	−0.2735	M_{tot}	36.88
a_{10}	0.068	C	0.8752	V_X	10
a_{01}	0.20	K_p	1	β_2	0.0098
a_{11}	2.14	K_v	1	β_3	0.0016
b_{00}	−0.038	T_v	0.02 s	β_4	0
b_{10}	−0.072	-	-	-	-

2.3. Hydrogen Supply System Model

The hydrogen supply system considered in this work consists of a high-pressure tank, a low-pressure tank, a gas compressor, and two solenoid valves, denoted as HV and LV, respectively. The thermodynamic behavior of the hydrogen stored in each of the pressure tanks is governed by Beattie–Bridgeman equation [25]. In Appendix A, the Beattie–Bridgeman equation is normalized to:

$$p_X = f_X(m_X) = T_X \left(\frac{m_X}{V_X} \right) + \sum_{k=2}^4 \beta_k \left(\frac{m_X}{V_X} \right)^k \quad (5)$$

where the gas pressure p_X in the tank is expressed as a fourth degree polynomial function $f_X(\cdot)$ of the hydrogen mass m_X . The subscript X can be H or L , which denote the high- or low-pressure tank respectively. V_X denotes the tank volume, and temperature T_X is assumed to be the same as the cold sink temperature T_k of the Stirling engine.

Fast-responding solenoid valves HV and LV are used to regulate the mean pressure p_{mean} of the hydrogen in the engine cylinder by controlling the mass exchange rate gA_{HV} and gA_{LV} respectively [11]. The control law, described by Equations (6) and (7), is such that if a positive valve command c is given, HV will open to allow hydrogen to flow into the cylinder while LV will close. This will increase both the mass and mean pressure of the hydrogen in the cylinder. Conversely, the reverse actions are taken for a negative command c . Thus,

$$T_v \frac{d(gA_{\text{HV}})}{dt} = \begin{cases} -gA_{\text{HV}} + K_v c, & c > 0 \\ 0, & c \leq 0 \end{cases} \quad (6)$$

$$T_v \frac{d(gA_{\text{LV}})}{dt} = \begin{cases} 0, & c > 0 \\ -gA_{\text{LV}} - K_v c, & c \leq 0 \end{cases} \quad (7)$$

In Equations (6) and (7), K_v and T_v are the gain and the time constant of the solenoid valves, respectively. As $p_H > p_{\text{mean}} > p_L$, hydrogen can only flow from the high- to the low-pressure tanks via the cylinder. As this flow continues, p_H will be decreasing while p_L will correspondingly increase. This is an unsustainable situation. A compressor is therefore used to maintain the gas pressures in the tanks at suitable levels. Considering the thermodynamic process to be a two-state polytropic compression, the power P_{comp} consumed by the compressor can be expressed as [25]:

$$P_{\text{comp}} = \frac{p_N T_N R}{P_{m,N} M} \frac{2T_{\text{comp}} n_c}{n_c - 1} \left[\left(\sqrt{\frac{p_H}{p_L}} \right)^{\frac{n_c - 1}{n_c}} - 1 \right] \frac{gA_{\text{comp}}}{\eta_{\text{comp}}} \quad (8)$$

where η_{comp} is the overall efficiency of the compressor, n_c is the polytropic constant, and the compressor temperature T_{comp} is assumed to be the same as the cold sink temperature T_k . gA_{comp} is the mass flow rate of the gas in the compressor. With the compressor in operation, the mass balance equations are:

$$\frac{dm_H}{dt} = gA_{comp} - gA_{HV} \tag{9}$$

$$\frac{dm_L}{dt} = gA_{LV} - gA_{comp} \tag{10}$$

$$m_{se} = M_{tot} - m_H - m_L \tag{11}$$

$$gA_{se} = gA_{HV} - gA_{LV} \tag{12}$$

where M_{tot} is the total mass of the hydrogen in the DS system.

The block diagram of the pneumatic model, containing Equations (5)–(12), of the hydrogen supply system is shown in Figure 3, and the parameters used in this work are given in Table 2. Note that the operation of the valves is limited by the maximum mass flow rate gA_{max} , as indicated in Figure 3.

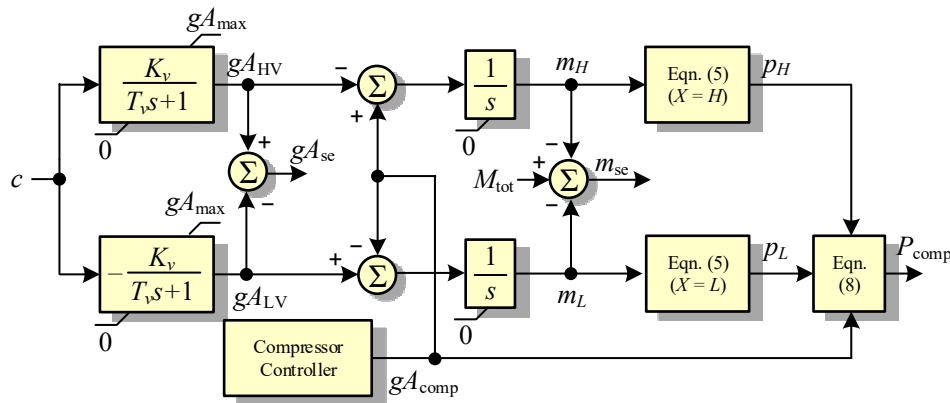


Figure 3. Block diagrams of the hydrogen supply system model including solenoid valves, pressure tanks, and gas compressor.

2.4. DFIG Model

For the time-domain simulation and control system design, a fifth-order induction machine model has been widely used [18,26]. Expressed in the synchronous reference frame, the voltage equations, flux linkage equations, and electromagnetic equation of this per-unit DFIG model are given as Equations (13)–(15), respectively:

$$\begin{cases} v_{ds} = -R_s i_{ds} + \psi_{qs} - \frac{1}{\omega_e} \frac{d\psi_{ds}}{dt} \\ v_{qs} = -R_s i_{qs} - \psi_{ds} - \frac{1}{\omega_e} \frac{d\psi_{qs}}{dt} \\ v_{dr} = -R_r i_{dr} + (1 - \omega_r) \psi_{qr} - \frac{1}{\omega_e} \frac{d\psi_{dr}}{dt} \\ v_{qr} = -R_r i_{qr} - (1 - \omega_r) \psi_{dr} - \frac{1}{\omega_e} \frac{d\psi_{qr}}{dt} \end{cases} \tag{13}$$

$$\begin{cases} \psi_{ds} = L_s i_{ds} + L_m i_{dr} \\ \psi_{qs} = L_s i_{qs} + L_m i_{qr} \\ \psi_{dr} = L_r i_{dr} + L_m i_{ds} \\ \psi_{qr} = L_r i_{qr} + L_m i_{qs} \end{cases} \tag{14}$$

$$T_e = L_m (i_{qr} i_{ds} - i_{dr} i_{qs}) \tag{15}$$

where v_{ds} and v_{qs} are d - and q -axis stator voltages, respectively; v_{dr} and v_{qr} are d - and q -axis rotor voltages, respectively; i_{ds} and i_{qs} are d - and q -axis stator currents, respectively; i_{dr} and i_{qr} are d - and q -axis rotor currents, respectively.

q -axis rotor currents, respectively; ψ_{ds} and ψ_{qs} are d - and q -axis stator flux linkages, respectively; ψ_{dr} and ψ_{qr} are d - and q -axis rotor flux linkages, respectively; R_s and R_r are the stator and rotor resistances; L_s , L_r , and L_m are the stator self-inductance, rotor self-inductance, and mutual inductance, respectively; ω_r is the shaft angular speed; and T_e is the electromagnetic torque T_e of the DFIG, respectively. Note that the generator convention is used and all the quantities are expressed in per-unit except the synchronous speed $\omega_e = 2\pi f$, where f is the nominal system frequency.

Moreover, the motion equation of the DFIG is:

$$2H \frac{d\omega_r}{dt} = T_m - T_e - D\omega_r \quad (16)$$

where H is the inertia constant of a one-mass lumped-parameter shaft model of the DFIG-based DS system and D is the damping constant. T_m is the mechanical torque of the DFIG. Note that the selected base values for angular speed and torque quantities of the DFIG per-unit system are different from those given in Table 1, and the following equations are used for unit conversion:

$$\omega_m = \frac{2\pi f_N / p_n}{\omega_{m,N}} \frac{1}{r_\omega} \omega_r \quad (17)$$

$$T_m = \frac{2\pi f_N / p_n}{S_N} \frac{P_{m,N}}{\omega_{m,N}} \frac{1}{r_\omega} \tau_m \quad (18)$$

where S_N is the nominal apparent power rating of the DFIG, p_n is the number of pole pairs of the DFIG, and r_ω represents the gearbox ratio.

Finally, taking the power P_{comp} consumed by the compressor into consideration, the total active power generated by the PCU is thus:

$$P_{PCU} = P_s + P_r - \frac{P_{m,N}}{S_N} P_{comp} = (v_{ds}i_{ds} + v_{qs}i_{qs}) + (v_{dr}i_{dr} + v_{qr}i_{qr}) - \frac{P_{m,N}}{S_N} P_{comp} \quad (19)$$

where P_s and P_r are the stator and rotor powers of the DFIG, respectively. The model parameters of DFIG used in this work are given in Table 3.

Table 3. DFIG model parameters.

Param.	Value	Param.	Value
S_N	30 kVA	L_m	2.9
f_N	60 Hz	H	0.685 s
R_s	0.0046	D	0.01
R_r	0.0032	p_n	2
L_s	3.08	r_ω	0.7614
L_r	3.06	-	-

3. Local Control System of the PCU

The design of the local control system for each PCU is presented in this section. There are three main control objectives under consideration, including (1) active power control, (2) receiver/absorber temperature control, and (3) tank pressure control. The study of the interaction between PCU and the grid system, including the reactive power and voltage control, is not the focus of the present investigation. Hence, we assume the DS system is connected to a single-machine infinite bus system and the terminal voltage at the point of connection is ideally maintained at the nominal voltage.

3.1. Direct Torque Control

For active power regulation, direct torque control (DTC) can simplify the procedure of controller design and reduce the parameter dependence of the system compared to the conventional voltage-modulated control schemes [27]. This approach is employed by taking advantage of the main features of this control concept, i.e., lower machine parameters dependency, simpler structure, no coordinate transformation, high dynamic performances, and minimal response time, which achieves better torque control conditions than field-oriented control.

The schematic of the DTC is shown in Figure 4. First, the measured three-phase rotor and stator currents are transformed into the components $i_{\alpha r}$, $i_{\beta r}$, $i_{\alpha s}$, and $i_{\beta s}$ in the two-phase stationary reference frame using a Clark transformation. The electromagnetic torque T_e , the magnitude Ψ_r and angle θ_{Ψ_r} of the rotor flux linkage are then estimated using Equations (20)–(22), respectively:

$$T_e = \psi_{\alpha r} i_{\beta r} - \psi_{\beta r} i_{\alpha r} \tag{20}$$

$$\psi_r = \sqrt{\psi_{\alpha r}^2 + \psi_{\beta r}^2} \tag{21}$$

$$\theta_{\psi_r} = \arctan(\psi_{\beta r} / \psi_{\alpha r}) \tag{22}$$

where $\psi_{\alpha s}$ and $\psi_{\beta s}$ are calculated using:

$$\begin{cases} \psi_{\alpha r} = L_r i_{\alpha r} + L_m i_{\alpha s} \\ \psi_{\beta r} = L_r i_{\beta r} + L_m i_{\beta s} \end{cases} \tag{23}$$

The estimated T_e is compared with the torque reference T_e^* obtained from the optimal torque control (OTC), which will be discussed in Section 3.2. The difference ΔT_e is used as the input of a three-level hysteresis comparator to generate the torque index K_T . Similarly, the estimated Ψ_r is compared with the flux reference Ψ_r^* to meet the requirement of reactive power control (which is not specifically discussed in this article). The difference $\Delta \Psi_r$ is sent to a two-level hysteresis comparator to generate the flux linkage index K_Ψ . Furthermore, θ_{Ψ_r} is used to determine the sector number K_S . The six gate signals for the RSC will be selected using a switching table based on the calculated combination of indices K_T , K_Ψ , and K_S . The detail of the implementation of DTC can be found in [27] and it is not elaborated on in this article.

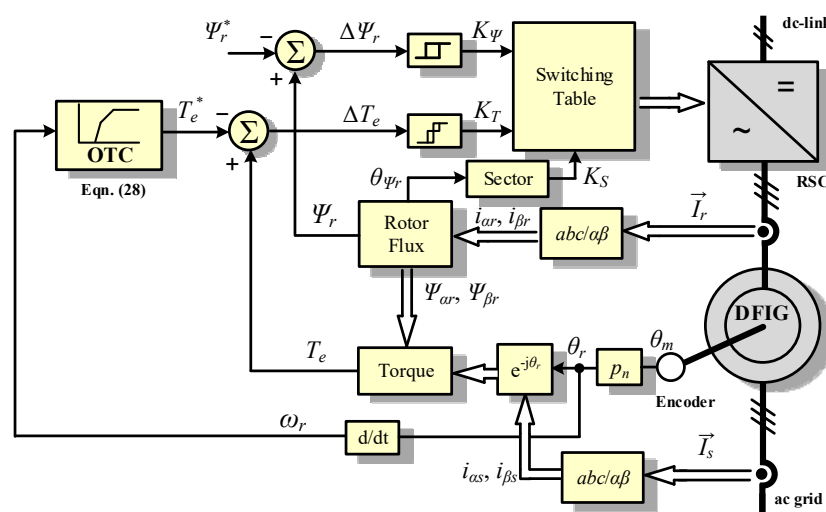


Figure 4. Schematic of the DFIG control.

3.2. Optimal Torque Control

The DTC introduced in the previous subsection decouples the regulation of the generated active power and the reactive power. By setting the torque reference T_e^* , the active power of the DFIG-based DS system can be regulated. In order to achieve MPPT, the steady-state analysis is conducted in this subsection to obtain the relationship between the optimal operating speed and the optimal torque.

First, using Equation (3), the steady-state mechanical torque τ_m of the engine can be expressed as:

$$\tau_m = \left(\frac{b_{00}}{\omega_m} + b_{01} + b_{02}\omega_m \right) + \left(\frac{b_{10}}{\omega_m} + b_{11} + b_{12}\omega_m \right) p_{\text{mean}} \quad (24)$$

Substituting Equation (2) into Equation (1) to eliminate Q_h , and setting $dT_h/dt = 0$ and $T_h = 1$ p.u. in the resulting equation, the steady-state mean pressure p_{mean} of the working gas can be expressed as a function of the insolation level I and the engine speed ω_m :

$$p_{\text{mean}} = \left(\frac{K_{\text{con}}I - (1 - T_a)/K_{\text{rec}} - (a_{00} + a_{01}\omega_m)}{a_{10} + a_{11}\omega_m} \right) \quad (25)$$

Next, substituting Equation (25) into Equation (24) to eliminate p_{mean} yields an expression of τ_m as a function of insolation level I and engine speed ω_m :

$$\tau_m = \left(\frac{b_{00}}{\omega_m} + b_{01} + b_{02}\omega_m \right) + \left(\frac{b_{10}}{\omega_m} + b_{11} + b_{12}\omega_m \right) \times \frac{K_{\text{con}}I - (1 - T_a)/K_{\text{rec}} - (a_{00} + a_{01}\omega_m)}{a_{10} + a_{11}\omega_m} \quad (26)$$

Using Equation (26), a family of τ_m versus ω_m curves at different insolation levels can be obtained and plotted, as shown in Figure 5. It can be seen that at the same insolation level, there is a decreasing trend in τ_m as the engine speed ω_m increases. In order to achieve the maximum energy harness, one can evaluate the engine power $P_m = \tau_m\omega_m$ at every insolation level, and the theoretical MPPT or OTC curve on the τ_m versus ω_m plane can then be obtained and shown as H-K in Figure 5.

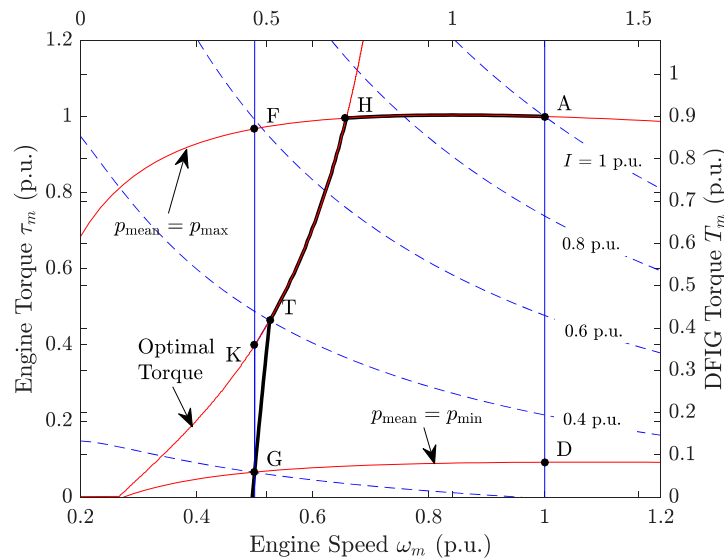


Figure 5. Optimal torque vs engine speed relationship.

However, the practical operation of the DS system is restricted by several physical limits. In Figure 5, these limits are indicated by: (a) the maximum mean pressure curve A-H ($p_{\text{mean}} = p_{\text{max}} = 1.0$ p.u.), (b) the minimum mean pressure curve D-G ($p_{\text{mean}} = p_{\text{min}}$), (c) the maximum insolation curve A-B ($I = 1.0$ p.u.), (d) the minimum speed limit F-G ($\omega_m = \omega_{m,\text{min}}$), and (e) the maximum speed limit B-C ($\omega_m = \omega_{m,\text{max}}$). Consequently, the feasible OTC curve becomes A-H-K-G, in which A-H and K-G are restricted by the maximum mean pressure of the working gas and the minimum engine speed,

respectively. As such, it is expected that the DS system can track A-H-K-G in order to extract as much power when insolation varies.

When implementing A-H-K-G in the control system, the torque reference shall be determined using the measured speed quantities. However, it can be seen that the torque is not uniquely determined by the speed when the system is operating on the minimum speed line G-K. Therefore, the tracking curve A-H-K-G is modified by replacing the constant speed line G-K with a ramp line G-T as shown in Figure 5. The revised feasible MPPT curve is thus A-H-T-G instead. The feasible optimal torque is thus expressed as a function f_{opt} of engine speed:

$$\tau_{m,opt} = f_{opt}(\omega_m) \tag{27}$$

Using Equations (16)–(18) and Equation (27), one can obtain the steady-state T_e versus ω_r relationship that will be used in the DFIG control system, as shown in Figure 4:

$$T_e^* = T_{e,opt} = \frac{2\pi f_N/p}{S_N} \frac{P_{m,N}}{\omega_{m,N}} f_{opt}\left(\frac{2\pi f_N/p}{\omega_{m,N}} \omega_r\right) - D\omega_r \tag{28}$$

3.3. Receiver/Absorber Temperature Control

Temperature control of a DS system is essential because it ensures the safe and efficient operation of the PCU. The receiver/absorber temperature T_h is anticipated to be as high as possible to increase the thermal efficiency (which is defined as the energy conversion efficiency from the absorbed heat transfer rate Q_h to the mechanical power P_m of the Stirling engine) of the Stirling engine, while the material of the receiver/absorber will be damaged if the maximum tolerable temperature is exceeded [11].

As explained in [19], to overcome the problems caused by speed variation and system nonlinearity in a variable-speed DS system, a fuzzy supervisory control can be designed by taking advantage of the relatively slow variation of the insolation. Several local temperature controllers are designed using the pole-placement method by linearizing the system model at several selected operating points. The supervisor determines the control decision c of the solenoid valves. Although effective, a large set of control parameters have to be tuned. The selection of suitable positions of poles are empirical due to the complex control structure. In this subsection, we propose a simple temperature control scheme and only three control parameters need to be determined. The schematic of the proposed temperature control system is shown in Figure 6.

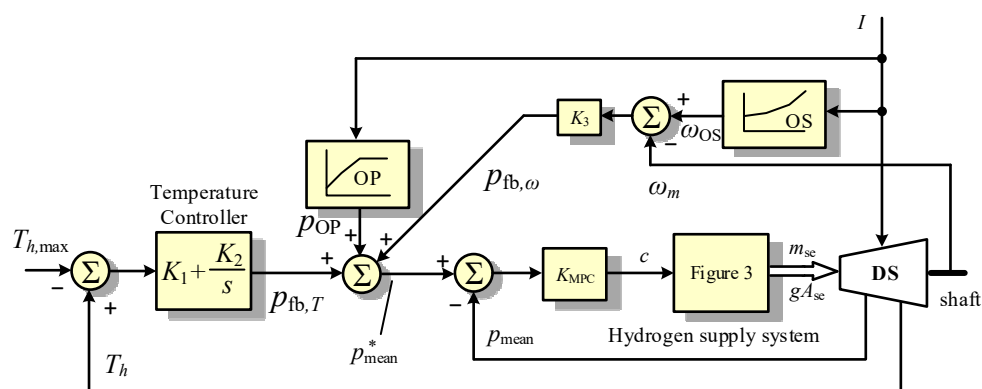


Figure 6. Schematic of the proposed prime mover control.

As shown in Figure 6, instead of using the pole placement method for the design of a state feedback controller, a mean pressure control (MPC) scheme for the conventional fixed-speed DS system is used here, which is expressed as [14]:

$$c = K_{MPC}(p_{mean}^* - p_{mean}) \tag{29}$$

where p_{mean}^* is the set-point of the mean pressure of the working gas, and K_{MPC} is the control gain of MPC. In order to reduce the negative impact of the disturbances of the varying insolation and speed, in the proposed temperature control scheme, the pressure set-point p_{mean}^* is expressed as:

$$p_{\text{mean}}^* = \overbrace{K_1(T_h - T_{h,\text{max}}) + K_2 \int (T_h - T_{h,\text{max}})dt}^{p_{\text{fb},T}} + p_{\text{OP}}(I) + \overbrace{K_3(\omega_{\text{OS}}(I) - \omega_m)}^{p_{\text{fb},\omega}} \quad (30)$$

Here p_{mean}^* consists of three components: $p_{\text{fb},T}$ is the output of the temperature PI controller, p_{OP} is the term for feedforward compensation of the disturbance due to the insolation variation, and $p_{\text{fb},\omega}$ is the term to compensate for the disturbance due to the speed variation.

The optimal mean pressure (OP) function $p_{\text{OP}}(I)$ and the optimal speed (OS) function $\omega_{\text{OS}}(I)$ depend on the steady-state p_{mean} versus I and ω_m versus I relationships, respectively, which can be predetermined analytically as follows. First, substituting Equation (27) into Equation (26) yields the ω_m versus I relationship. Next, using this ω_m versus I relationship and Equation (25) gives the p_{mean} versus I relationship. These relationships are shown in Figure 7 and they can be implemented using two look-up tables.

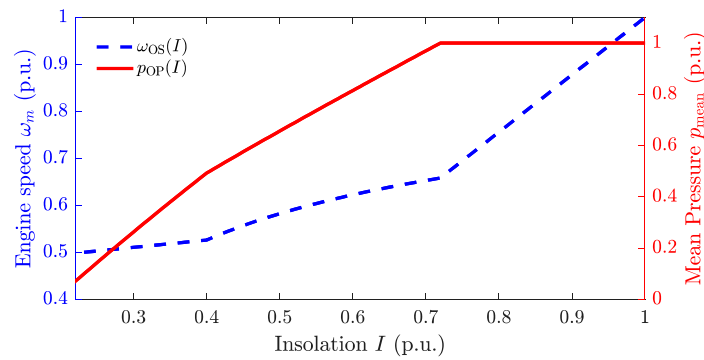


Figure 7. Steady-state p_{mean} vs. I and ω_m vs. I relationships.

3.4. Tank Pressure Control

Moreover, as shown in Figure 3, the compressor shall be used to maintain the tank pressure. The control law is expressed as:

$$gA_{\text{comp}} = K_4(p_H^* - p_H) \quad (31)$$

Hence, it can be seen that only four control parameters K_1 , K_2 , K_3 , and K_4 are required to be determined in Equations (30) and (31). The selection of the optimal control parameters will be determined using the PSO method in the next section.

4. Determination of Control Parameters

4.1. Constraints on Temperature Control Parameters

To determine the optimal control parameters, model order reduction is done first to simplify the stability analysis and to reduce the simulation time. First, to study the stability of the temperature control system, the effects of the compressor and pressure tanks are ignored by setting $gA_{\text{comp}} = 0$ and $P_{\text{comp}} = 0$. In doing so, the hydrogen supply system model described using Equations (5)–(12) collapses to that shown in [19]:

$$T_v \frac{d(gA_{\text{se}})}{dt} = -gA_{\text{se}} + K_v c \quad (32)$$

$$\frac{dp_{\text{mean}}}{dt} = K_p (gA_{\text{se}}) \quad (33)$$

Applying the Routh–Hurwitz stability criterion to Equation (35) gives the following Constraints (36)–(38):

$$0 < K_1 < \frac{T'_{rec}}{T_{se1}K_{rec}K_{hp}} \tag{36}$$

$$-\frac{(D'' + K_3) + K_{rec}K_1(D''K_{hp} + K_{mp}K_{hw})}{K_{rec}K_{hp}(2H - T_{se1}D'')} < K_2 < \frac{2H + (D'' + K_3)T'_{rec} + K_{rec}K_{hp}(2H - T_{se1}D'')K_1}{2HT_{se1}K_{rec}K_{hp}} \tag{37}$$

$$\begin{aligned} & \left(2H + (D'' + K_3)T'_{rec} + K_{rec}K_{hp}(2H - T_{se1}D'')K_1 - 2HT_{se1}K_{rec}K_{hp}K_2 \right) \times \\ & \left((D'' + K_3) + K_{rec}K_1(D''K_{hp} + K_{mp}K_{hw}) + K_{rec}K_{hp}(2H - T_{se1}D'')K_2 \right) > \\ & 2HK_{rec}K_2(T'_{rec} - T_{se1}K_{rec}K_{hp}K_1)(D''K_{hp} + K_{mp}K_{hw}) \end{aligned} \tag{38}$$

Constraints (36)–(38) will be used as constraints in the next subsection for particle swarm optimization to determine the optimal control parameters.

4.2. Particle Swarm Optimization

In the present investigation, the control objective is to maximize the energy generation, while maintain the operating temperature at a suitable level. Moreover, the hydrogen pressure in the tanks shall be maintained. For a given insolation profile $I(t)$, we formulate the selection of control parameters as a finite horizon constrained optimization problem:

$$\min_{K_1, K_2, K_3, K_4} J = \min_{K_1, K_2, K_3, K_4} \left\{ - \int_0^{t_{max}} P_{PCU}(t)dt + \varphi_1(T_h(t)) + \varphi_2(p_H(t_{max})) \right\} \tag{39}$$

subject to system model using Equations (1)–(19) and Constraints (36)–(38). In Constraint (39), the first term represents the total generated energy, φ_1 is used to implement a state constraint to limit the temperature within a narrow band $|T_h - T_{h,max}| \leq \Delta T_{h,max}$, and φ_2 is used to introduce an additional cost to make sure that the final value of the tank pressure p_H restores to its set-point. They are expressed as:

$$\varphi_1(T_h(t)) = \alpha \int_0^{t_{max}} \max\{T_{h,max} - \Delta T_{h,max} - T_h(t), 0, T_h(t) - T_{h,max} - \Delta T_{h,max}\} dt \tag{40}$$

$$\varphi_2(p_H(t_{max})) = \beta \max\{p_H^* - \Delta p_{H,max} - p_H(t_{max}), 0\} \tag{41}$$

where α and β are the penalty coefficients with large values. To obtain the cost J for each combination of control parameters (i.e., each particle), time-domain simulation has to be carried out. In order to reduce the searching time, the system model of Equations (1)–(19) will be simplified by assuming that the electromagnetic torque is ideally controlled using a DTC and no converter dynamics are considered, which yields $\tau_e = \tau_e^*$. Next, representing Equation (16) in the per unit system of the prime mover and considering Equation (27), thus gives:

$$2H' \frac{d\omega_m}{dt} = \tau_m - \tau_e^* - D'\omega_m = \tau_m - f_{opt}(\omega_m) \tag{42}$$

where H' and D' are converted from H and D as given in Table 3. The PCU power Equation (19) is therefore modified to give:

$$P_{PCU} = \eta(I)T_e\omega_r - \frac{P_{m,N}}{S_N}P_{comp} = \frac{P_{m,N}}{S_N}(\eta(I)\tau_e\omega_m - P_{comp}) \tag{43}$$

where η is a coefficient considering the losses in the DFIG windings, and it is expressed as a function of insolation I . Hence, the reduced order model for optimization algorithm design shall consists of Equations (1)–(12), (29)–(31), (42), and (43). Here we denote this model as the *PSO-ROM*.

In Equation (39), t_{\max} is the time horizon of the insolation profile. Parameters α and β are penalties for the evaluation of the performance of active power regulation and temperature control, respectively.

PSO is a simple and effective metaheuristic optimization technique that is initialized with some population of random candidates and a search algorithm to reach the global optimum for the defined objective function [28]. In an n -dimensional optimization problem, the position vector $\mathbf{x} \in \mathbb{R}^n$ and velocity vector $\mathbf{v} \in \mathbb{R}^n$ of the i -th particle in the iteration number j are expressed as:

$$\mathbf{x}_i^j = [x_{i,1}^j \quad x_{i,2}^j \quad \cdots \quad x_{i,n}^j] \quad (44)$$

$$\mathbf{v}_i^j = [v_{i,1}^j \quad v_{i,2}^j \quad \cdots \quad v_{i,n}^j] \quad (45)$$

Each position vector represents a potential solution to the problem, while the velocity vector indicates the extent of variation in the updating procedure. The equations with which the velocity and the positions of the particles are updated are:

$$\mathbf{v}_i^{j+1} = w\mathbf{v}_i^j + c_1r_i^j(\mathbf{p}_i^j - \mathbf{x}_i^j) + c_2s_i^j(\mathbf{g}^j - \mathbf{x}_i^j) \quad (46)$$

$$\mathbf{x}_i^{j+1} = \mathbf{x}_i^j + \mathbf{v}_i^{j+1} \quad (47)$$

where p is the recorded best solution for specific particle and g is the global optimal solution among all p . r and s are two random numbers between 0 and 1. w , c_1 , and c_2 are referred as the inertia constant, cognitive scaling parameter, and social scaling parameter, respectively. The recommended values $c_1 = c_2 = 2$ in [29] are used in this article and w is selected to be 0.8. These coefficients determine how much of each component from the previous iteration affects the next movement of the algorithm.

For the problem in hand, the position vector is a four-dimensional vector:

$$\mathbf{x} = [K_1 \quad K_2 \quad K_3 \quad K_4] \quad (48)$$

For the control scheme proposed in [19], there are 20 control parameters that need to be determined: 18 for the temperature controller and 2 for the speed controller. Hence, the number of control parameters have been significantly reduced.

In this article, the values of K_1 , K_2 , and K_3 shall satisfy Constraints (36)–(38). Hence, during the step to randomly select the particle, an additional step will be included to examine the stability requirement. Unaccepted particles will be abandoned before conducting the time-domain simulation.

However, as most of the parametric values of the gains in the linearized model depends on the insolation level I , the feasible range of K_1 , K_2 , and K_3 varies. To illustrate this point, in Figure 9 we plot an example of the feasible search subspace $(K_1, K_2) \in \mathbb{R}^2$ when $K_3 = 0$. It can be observed that as the insolation increases, the maximum K_1 also increases, which can be derived from Constraint (36). The other boundary also moves which is governed by Constraints (37) and (38). To guarantee system stability, the search subspace shall be shared area under all insolation levels. However, considering that all the gains change smoothly, only the cases for the maximum and the minimum insolation are investigated for simplicity. The feasible search subspace is therefore obtained and shown as the shaded area in Figure 9.

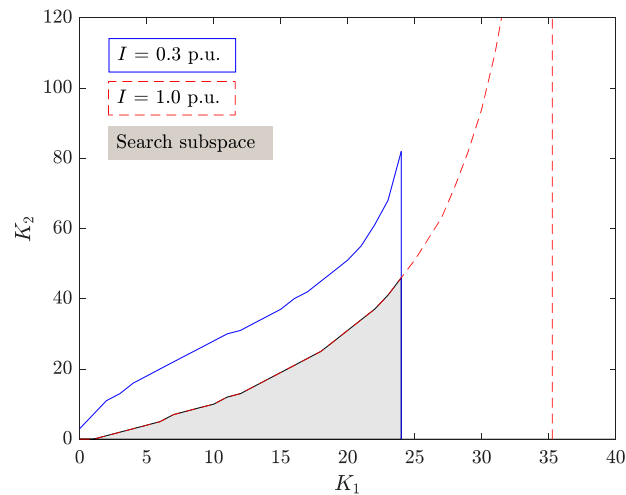


Figure 9. Feasible search subspace for PSO to determine K_1 and K_2 for $K_3 = 0$.

5. Results and Discussion

5.1. Model Validation and Comparison

In order to validate the accuracy of the proposed model, in this subsection, the simulation results from the developed model were compared with that obtained using the existing models. All the models were implemented and solved using MATLAB R2016a/Simulink 8.7 (The MathWorks, Inc., Natick, MA, USA). The parameters of the system model used in the simulation are given in Tables 1–3. The optimal control parameters obtained in the latter subsection are used.

First, for the Stirling engine, a multi-cylinder adiabatic model of the Stirling engine was used as the benchmark to evaluate the model accuracy of proposed model of Equations (1)–(19). This adiabatic model describes the thermodynamic cycles of four series-connected cylinders, and has been studied intensively in existing literature [11,12,21]. In this case, detailed representation of the converters and the grid system were established using the SymPowerSystems Toolbox. Figure 10 shows the simulation results when a step increase of insolation from 0.6 to 0.65 p.u. occurred at 0.5 s. The purpose was to compare the dynamic response of the models that could affect the stability of the system. It can be seen that using the average-value Stirling engine model, the dynamic behavior of the benchmark model could be successfully captured, while the high-frequency oscillating components in Figure 10c had an ignorable effect on other variables. This is in line with the conclusion of Reference [24]. Furthermore, the simulation results using an assumed prime mover model used in [18] are also presented. This model assumes the prime mover of the DS system is a first-order system and it ignores the detailed description of the thermodynamics of the Stirling engine and temperature control system. The mechanical torque was calculated according to the measured rotational speed of DFIG and insolation, according to the relationship presented in Figure 5. Corresponding temperature and absorbed heat transfer rate are not shown in Figure 10a,c as these variables are not considered in this assumed model. Clearly, it cannot reflect the dynamic characteristics of the DS system for the design of the temperature control system.

The effect of the tank volume V_X was investigated next and the proposed hydrogen supply system model was compared with the simplified model used in References [12,19] (i.e., Equations (32) and (33)). The simplified model ignores the detailed representation of the tank and compressor, which leads to $V_X = +\infty$ and $P_{\text{comp}} = 0$. In this case, the initial insolation level was 0.3 p.u., and it started to increase at 5 s with a ramp rate of 30 W/(m²·s) or 0.03 p.u./s. This value has been considered to be very fast for solar power generation studies [14]. Figure 11 shows the simulation results. A low-pass filter has been applied to the PCU power to remove the high-frequency components. From Figure 11b,d, it can be seen that for $V_X = 5.5$ p.u., the gas pressure in the low pressure tank reached zero during the transient, and a large amount of power was consumed by the compressor from 5 s to 20 s. By increasing the tank volume, the P_{comp} profile became flatter. For $V_X = 500$ p.u.,

the simulation results were close to that of the simplified model. Hence, when designing the optimal control scheme, the effect of the pressure tank and gas compressor should be carefully considered to improve the model accuracy.

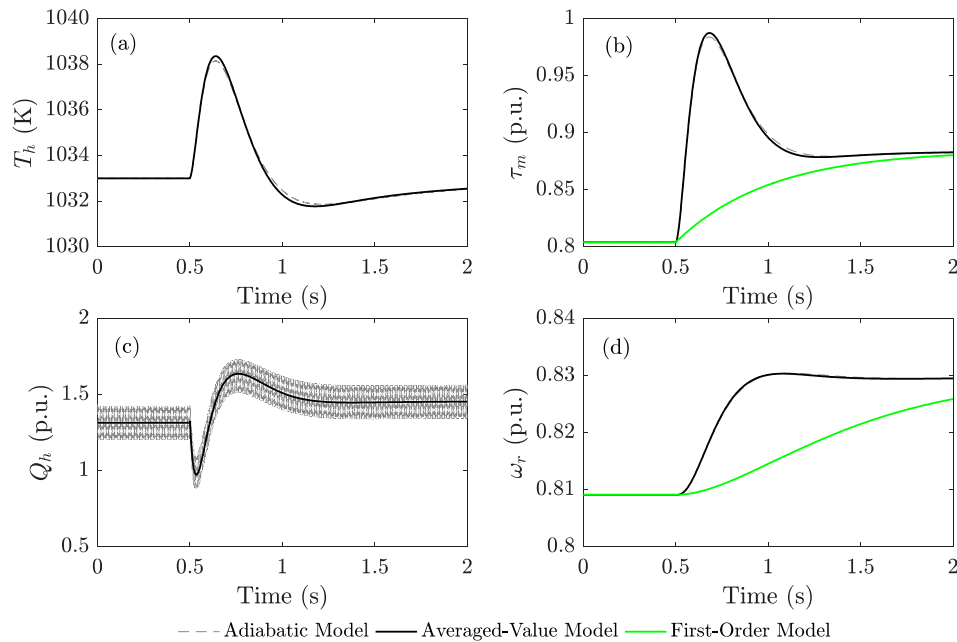


Figure 10. Comparison of simulation results with different Stirling engine model in response to a step change of insolation: (a) receiver temperature, (b) mechanical torque of the Stirling engine, (c) absorbed heat transfer rate of the Stirling engine, and (d) rotational speed of the DFIG.

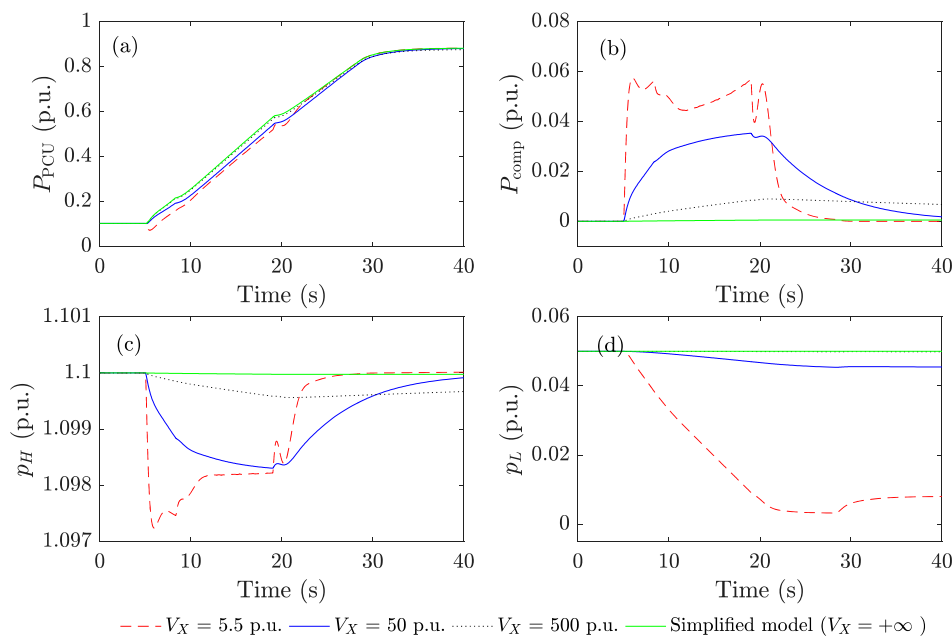


Figure 11. Comparison of simulation results using a different hydrogen supply system model with different tank volumes: (a) power generated by the PCU, (b) power consumed by the gas compressor, (c) gas pressure in the high pressure tank, and (d) gas pressure in the low pressure tank.

Furthermore, the proposed control scheme described in Section 3 was compared with an existing scheme proposed in [19]. In [19], MPPT was achieved using a classic double-loop control structure, with the outer feedback speed control loop and the inner current control loop. Space-vector pulse width

modulation (SVPWM) was used to generate the gate signal for the converter. Detail of such a scheme can be found in most textbooks and thus it is not elaborated on here. Figure 12 shows the simulation results. Again, low-pass filters have been applied to the PCU power and electromagnetic torque.

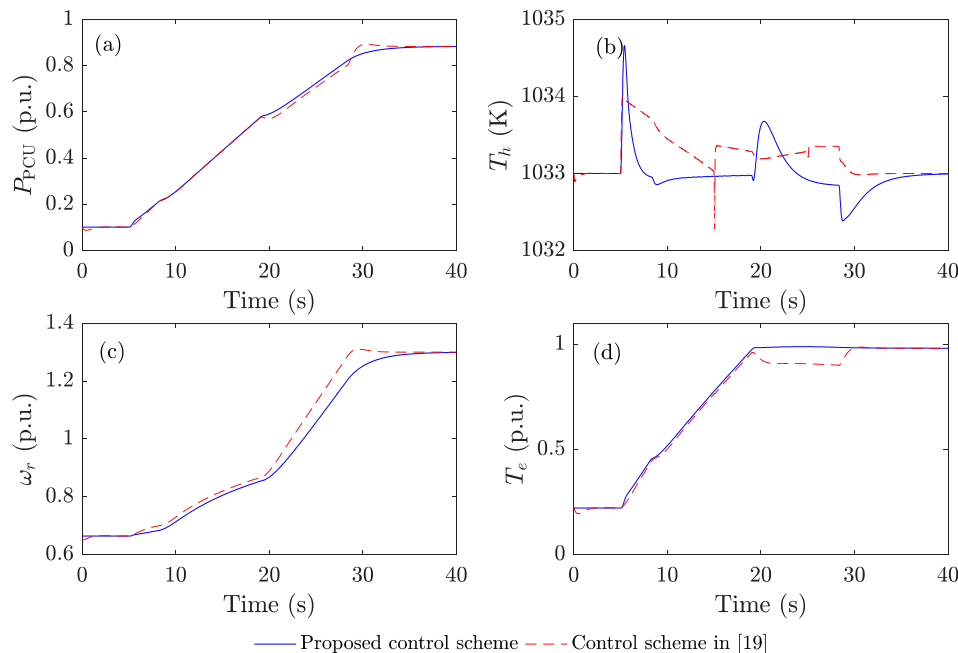


Figure 12. Comparison of different control schemes under a ramped increase of insolation: (a) power generated from PCU, (b) receiver temperature, (c) rotational speed of the DFIG, and (d) electromagnetic torque of the DFIG.

It can be seen from Figure 12b that for both schemes, the receiver temperature can be effectively regulated around the set-point 1033 K. However, Figure 12a shows that the proposed control scheme provides a smoothed power profile as insolation changes. The reason is explained briefly as follows. For the feedback speed control, in order to track the maximum power points during the insolation increase, an accelerating torque has to be provided. In Figure 12c, a higher ramp rate of speed is observed from 20 s to 30 s, compared to that before 20 s. This was due to the steady-state characteristics of the MPPT curve given in Figure 5. Hence, during this period, the control system had to reduce the electromagnetic torque of the DFIG so that more accelerating torque could be provided, and this could be observed from Figure 12d. Meanwhile, for the proposed DTC scheme, the torque is directly regulated according to the measured insolation, such that an unexpected decrease in electromagnetic torque can be effectively avoided, resulting in a flatter speed profile, as shown in Figure 12c.

5.2. Case Study

This section will present a case study where the simulation results were obtained from MATLAB/Simulink software. In this case study, the following 100-second insolation profile $I(t)$ was used for PSO: the initial insolation was 0.25 p.u. and the insolation was ramped up to the maximum insolation level 1.0 p.u. and then ramped down back to 0.25 p.u. The global optimal solution and the corresponding cost for each iteration are shown in Figure 13. Here, the particle size was 20. From Figure 13, it can be seen that the result converged and became stable at the 18th iteration, and the optimal control parameters were found to be $K_1 = 11.1$, $K_2 = 11.8$, $K_3 = 0.18$, and $K_4 = 25.5$.

Figure 14 shows the positions of the randomly generated particles using PSO at iteration 1, 2, 11, 12, 20, and 21. Note that only two dimensions (K_1 , K_2) are shown. It can be seen that the generated particles were approaching the optimal position as iterations increased, and all the particles fell within the feasible search subspace shown in Figure 9.

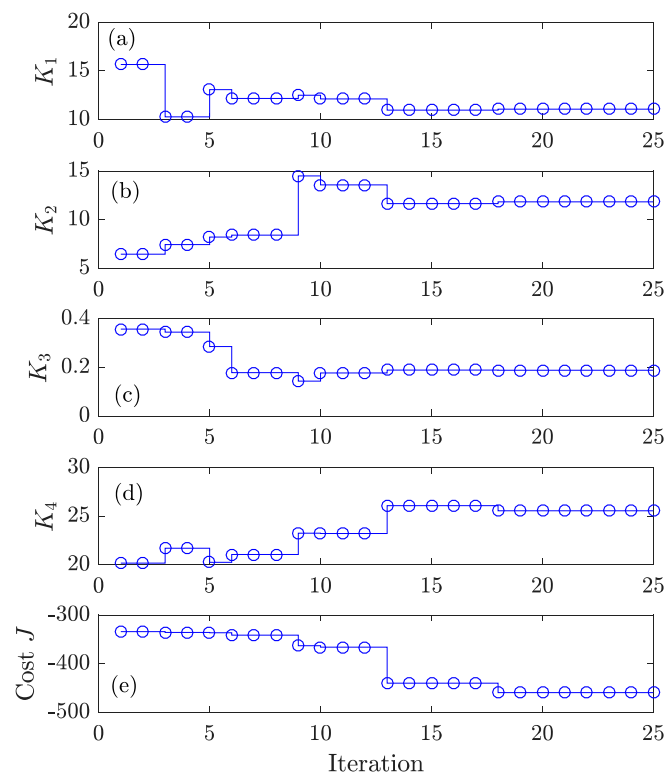


Figure 13. The global optimal solution and cost for each iteration. (a) K_1 vs. iteration number, (b) K_2 vs. iteration number, (c) K_3 vs. iteration number, (d) K_4 vs. iteration number, and (e) Cost function J vs. iteration number.

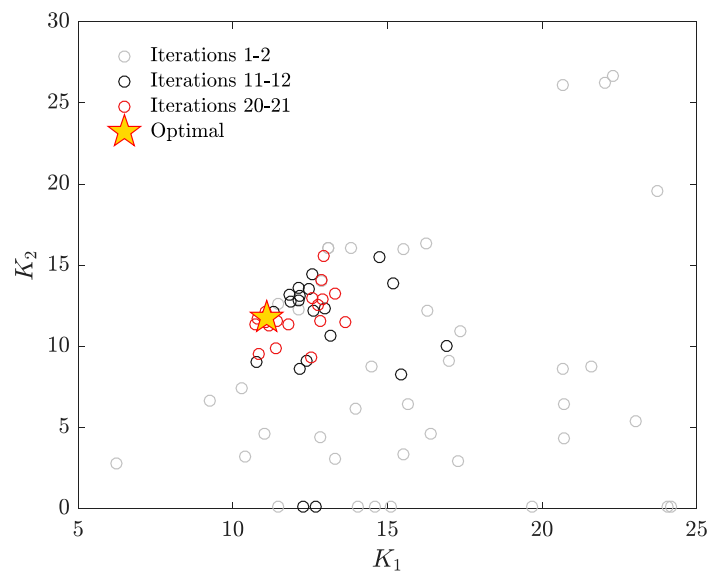


Figure 14. Positions of the particles at different iteration steps. Only two dimensions (K_1, K_2) are shown.

In order to show the efficacy of the obtained optimal control parameters, in Figure 15 we compare the simulation waveforms of the temperature T_h , PCU power P_{PCU} , compressor power P_{comp} , and the tank pressures p_H and p_L using four groups of different control parameters, including the optimal one and three other groups of parameters. As each group of the parameters can be considered as a particle in the PSO search space, we denoted the control parameters as Particle 1, Particle 2, and Particle 3, respectively. The parametric values of the three particles were selected to be:

- Particle 1: $K_1 = 20, K_2 = 11.8, K_3 = 0.18,$ and $K_4 = 25.5$.

- Particle 2: $K_1 = 11.1$, $K_2 = 11.8$, $K_3 = 0.18$, and $K_4 = 0.03$.
- Particle 3: $K_1 = 11.1$, $K_2 = 11.8$, $K_3 = 0.18$, and $K_4 = 100$.

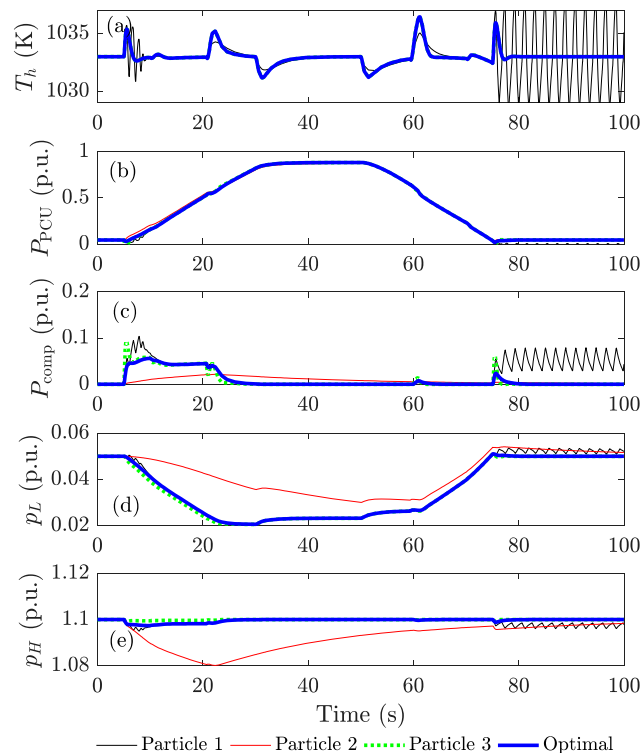


Figure 15. Simulation results with different particles (control parameters): (a) receiver temperature, (b) power generated from the PCU, (c) power consumed by the compressor, (d) gas pressure in the high pressure tank, and (e) gas pressure in the low pressure tank.

From Figure 15a, it can be seen that the temperature profiles from all four selected particles were limited within a narrow band between 1030 K (0.997 p.u) to 1036 K (1.003 p.u.). For the first particle, the system was unstable and the temperature was oscillating after the system reached the steady state after about 77 s. In the steady state, the compressor did not work and no power was being consumed by the compressor. However, it can be seen from Figure 15c that for the first particle, there is a persistent compressor power. The pressure in the high-pressure tank decreased and the pressure in the low-pressure tank increased, which can be observed from Figure 15d,e, respectively. Figure 15c shows the second particle consumed the least amount of compressor power, which helped to increase the total generated power from the PCU. However, from Figure 10e, it can be seen that at 100 s, the gas pressure in the high-pressure tank had not reached the set-point. For the third particle, although it provided a better control on the high pressure tank, it consumed more compressor power during the period of investigation.

6. Conclusions

This paper proposes an optimal control system design approach for a DFIG-based dish-Stirling concentrated solar-thermal generating system, aiming to achieve maximum power point tracking and constant temperature regulation. The overall system model with multi-physics nature has been developed for time-domain simulation studies in a grid-connected condition. The model incorporates an average-valued thermodynamic model of Stirling engine, a heat transfer model of the dish/receiver, and a pneumatic model of the hydrogen supply system. A coordinated torque and mean pressure control scheme were proposed to provide smoothed active power tracking and temperature regulation. This scheme requires tuning for only four control parameters, which is a significant

reduction from 20 in the existing literature. The optimal control parameters were determined using the PSO method, and the process of the pre-examination of system stability was incorporated into the algorithm to effectively reduce the search effort. The results from the time-domain simulation were presented to show the efficacy of the proposed scheme in supplying the grid system with improved performance of active power and temperature regulation as solar irradiance varied. It also showed the importance of the detailed modeling of the hydrogen supply system as the parasitic loss due to the gas compressor and the limited tank volume can play negative impact on the energy conversion efficiency, which should be taken into consideration during the design of the DS system.

Author Contributions: Conceptualization, Y.L.; methodology, Y.L. and B.X.; software, Y.L. and Z.L.; validation, Y.L. and Z.L.; investigation, B.X.; writing—original draft preparation, Y.L.; writing—review and editing, Y.S. and J.T.; supervision, Y.L. and Y.S.; project administration, B.X.; funding acquisition, B.X.

Funding: This work was supported by National Natural Science Foundation of China (#61703318), Natural Science Foundation of Hubei Province (#2017CFB130), and Open Fund of State Key Laboratory of Operation and Control of Renewable Energy & Storage Systems (#DGB51201801584).

Conflicts of Interest: The authors declare no conflict of interest.

Nomenclature

D, H	damping and inertia constants of DS system (p.u. in electrical system)
D', H'	damping and inertia constants of DS system (p.u. in mechanical system)
$I(t)$	solar insolation (p.u.)
K_1, K_2	proportional and integral gains of the temperature controller
K_3	gain of the speed feedforward controller
K_4	gain of the hydrogen compressor controller
K_v, T_v	gain and time constant of solenoid valve
K_{con}	gain of the concentrator
K_{rec}, T_{rec}	gain and time constant of receiver
K_p	engine pressure–mass gain
M_{tot}	total mass in the engine cylinders
$P_e(t), P_m(t)$	electromagnetic power, mechanical power (p.u.)
$P_{comp}(t)$	power consumed by the hydrogen compressor (p.u.)
$P_{PCU}(t)$	power generated from PCU (p.u.)
$Q_h(t)$	heater and cooler heat transfer rate (p.u.).
T_a	ambient temperature (p.u.)
$T_e(t), T_m(t)$	electromagnetic and mechanical torques (p.u. in electrical system)
$T_h(t)$	heater/receiver temperature (p.u.)
$a_{00}, a_{01}, a_{10}, a_{11}$	steady-state efficiency correction coefficients of Stirling engine
$b_{00}, b_{01}, b_{10}, b_{11}, b_{02}, b_{12}$	
$c(t)$	control command of solenoid valve (p.u.)
$gA_{se}(t)$	total mass flow rate from tanks to engine cylinder (p.u.)
$m_{se}(t)$	mass of the hydrogen in the engine cylinder
$m_H(t), m_L(t)$	masses of the hydrogen in the high- and low-pressure tanks (p.u.)
$p_{mean}(t)$	mean pressure of the working gas in the Stirling engine cylinder (p.u.)
p_{max}, p_{min}	maximum and minimum pressure in the Stirling engine cylinder (p.u.)
$p_H(t), p_L(t)$	pressures of the hydrogen in the high- and low-pressure tanks (p.u.)
$\tau_e(t), \tau_m(t)$	electromagnetic and mechanical torques (p.u. in mechanical system)
$\omega_m(t)$	shaft speed of engine/generator (p.u. in mechanical system)
$\omega_r(t)$	shaft speed of engine/generator (p.u. in electrical system)

Appendix A

The original Beattie–Bridgeman equation is given in [25] is:

$$p = \frac{n^2 RT}{V^2} \left(1 - \frac{c_0 n}{VT^3} \right) \left[\frac{V}{n} + B_0 \left(1 - b_0 \frac{n}{V} \right) \right] - A_0 \left(1 - a_0 \frac{n}{V} \right) \left(\frac{n}{V} \right)^2 \quad (\text{A1})$$

where $n = m/M$ is the amount of the substance, and m is the mass and M is the molar mass of hydrogen. The units of the states of the equation are: p (atm), n (mol), m (kg), V (L), T (K). By using the base values given in Table 1, Equation (A1) can be normalized to:

$$p_X(m_X) = R'T_X \left(\frac{m_X}{V_X} \right)^2 \left(1 - \frac{c'_0}{T_X^3} \frac{m_X}{V_X} \right) \left[\frac{V_X}{m_X} + B'_0 \left(1 - b'_0 \frac{m_X}{V_X} \right) \right] - A'_0 \left(1 - a'_0 \frac{m_X}{V_X} \right) \left(\frac{m_X}{V_X} \right)^2 \quad (\text{A2})$$

where the hydrogen constants are:

$$\begin{aligned} R' &= \frac{Rm_N T_N}{p_N M V_N}, A'_0 = \frac{m_N^2}{p_N M^2 V_N^2} A_0, B'_0 = \frac{m_N}{M V_N} B_0, \\ a'_0 &= \frac{m_N}{M V_N} a_0, b'_0 = \frac{m_N}{M V_N} b_0, c'_0 = \frac{m_N}{M V_N T_N^3} c_0 \end{aligned} \quad (\text{A3})$$

Re-arranging Equation (A2) yields Equation (5), where the coefficients β_k are:

$$\begin{aligned} \beta_2 &= B'_0 T_X - c'_0 / T_X^2 - A'_0 \\ \beta_3 &= A'_0 a'_0 b'_0 - B'_0 b'_0 T_X - c'_0 B'_0 / T_X^2 \\ \beta_4 &= c'_0 B'_0 b'_0 / T_X^2 \end{aligned} \quad (\text{A4})$$

The hydrogen constants used in Equation (A1) are: $R = 0.08206 \text{ atm}\cdot\text{L}/(\text{mol}\cdot\text{K})$, $A_0 = 0.1975 \text{ atm L}^2/\text{mol}^2$, $B_0 = 0.02096 \text{ L}/\text{mol}$, $a_0 = -0.00506 \text{ L}/\text{mol}$, $b_0 = -0.04359 \text{ L}/\text{mol}$, $c_0 = 504 \text{ L}\cdot\text{K}^3/\text{mol}$, and $M = 2015.88 \text{ kg}/\text{mol}$. The normalized hydrogen constants used in Equation (A2) are: $R' = 1$, $A'_0 = 0.0054$, $B'_0 = 0.0489$, $a'_0 = -0.0118$, $b'_0 = -0.1016$, and $c'_0 \approx 0$.

References

- Mancini, T.; Heller, P.; Butler, B.; Osborn, B.; Schiel, W.; Goldberg, V.; Buck, R.; Diver, R.; Andraka, C.; Moreno, J. Dish-Stirling systems: An overview of development and status. *ASME J. Sol. Energy Eng.* **2003**, *125*, 135–151. [[CrossRef](#)]
- Thombare, D.G.; Verma, S.K. Technological development in the Stirling cycle engines. *Renew. Sustain. Energy Rev.* **2008**, *12*, 1–38. [[CrossRef](#)]
- Mendoza Castellanos, L.S.; Carrillo Caballero, G.E.; Melian Cobas, V.R.; Silva Lora, E.E.; Martinez Reyes, A.M. Mathematical modeling of the geometrical sizing and thermal performance of a Dish/Stirling system for power generation. *Renew. Energy* **2017**, *107*, 23–35. [[CrossRef](#)]
- Mendoza Castellanos, L.S.; Galindo Noguera, A.L.; Carrillo Caballero, G.E.; De Souza, A.L.; Melian Cobas, V.R.; Silva Lora, E.E.; Venturini, O.J. Experimental analysis and numerical validation of the solar Dish/Stirling system connected to the electric grid. *Renew. Energy* **2019**, *135*, 259–265. [[CrossRef](#)]
- Gholamalizadeh, E.; Chung, J.D. Thermal Analysis of the Receiver of a Standalone Pilot Solar Dish–Stirling System. *Entropy* **2018**, *20*, 429. [[CrossRef](#)]
- Gil, R.; Monné, C.; Bernal, N.; Muñoz, M.; Moreno, F. Thermal Model of a Dish Stirling Cavity-Receiver. *Energies* **2015**, *8*, 1042–1057. [[CrossRef](#)]
- Sandoval, O.R.; Caetano, B.C.; Borges, M.U.; García, J.J.; Valle, R.M. Modelling, simulation and thermal analysis of a solar dish/Stirling system: A case study in Natal, Brazil. *Energy Convers. Manag.* **2019**, *181*, 189–201. [[CrossRef](#)]
- Zhu, S.; Yu, G.; Jongmin, O.; Xu, T.; Wu, Z.; Dai, W.; Luo, E. Modeling and experimental investigation of a free-piston Stirling engine-based micro-combined heat and power system. *Appl. Energy* **2018**, *226*, 522–533. [[CrossRef](#)]
- Wu, Z.; Jin, J.X. Novel concept of dish Stirling solar power generation designed with a HTS linear generator. *IEEE Trans. Appl. Supercond.* **2014**, *24*, 5203005. [[CrossRef](#)]
- Qiu, S.; Solomon, L.; Rinker, G. Development of an Integrated Thermal Energy Storage and Free-Piston Stirling Generator for a Concentrating Solar Power System. *Energies* **2017**, *10*, 1361. [[CrossRef](#)]
- Howard, D.F.; Liang, J.; Harley, R.G. Control of receiver temperature and shaft speed in dish-Stirling solar power plants to meet grid integration requirements. In Proceedings of the IEEE Energy Conversion Congress and Exposition, Atlanta, GA, USA, 12–16 September 2010; pp. 398–405.
- Howard, D.; Harley, R.G. Modeling of dish-Stirling solar thermal power generation. In Proceedings of the IEEE PES General Meeting, Providence, RI, USA, 25–29 July 2010.

13. Urieli, I.; Berchowitz, D.M. *Stirling Cycle Engine Analysis*; A. Hilger: Bristol, UK, 1984.
14. Li, Y.; Choi, S.S.; Yang, C. Dish-Stirling solar power plants: Modeling, analysis and control of receiver temperature. *IEEE Trans. Sustain. Energy* **2014**, *5*, 398–407. [[CrossRef](#)]
15. Li, Y.; Choi, S.S.; Vilathgamuwa, D.M. Primary frequency control scheme for a fixed-speed dish-stirling solar-thermal power plant. *IEEE Trans. Power Syst.* **2018**, *33*, 2184–2194. [[CrossRef](#)]
16. Hussain, I.; Das, D.C.; Sinha, N. Reactive power performance analysis of dish-Stirling solar thermal-diesel hybrid energy system. *IET Renew. Power Gen.* **2017**, *11*, 750–762. [[CrossRef](#)]
17. Howard, D.F.; Harley, R.G.; Jiaqi, L.; Venayagamoorthy, G.K. Effects of variable solar irradiance on the reactive power compensation for large solar farm. In Proceedings of the IREP Symposium—Bulk Power System Dynamics and Control, Rio de Janeiro, Brazil, 1–6 August 2010; pp. 1–8.
18. Santos-Martin, D.; Alonso-Martinez, J.; Eloy-Garcia, J.; Arnalte, S. Solar dish-Stirling system optimisation with a doubly fed induction generator. *IET Renew. Power Gen.* **2012**, *6*, 276–288. [[CrossRef](#)]
19. Li, Y.; Choi, S.S.; Yang, C.; Wei, F. Design of variable-speed dish-Stirling solar-thermal power plant for maximum energy harness. *IEEE Trans. Energy Convers.* **2015**, *30*, 394–403. [[CrossRef](#)]
20. Barreto, G.; Canhoto, P. Modelling of a Stirling engine with parabolic dish for thermal to electric conversion of solar energy. *Energy Convers. Manag.* **2017**, *132*, 119–135. [[CrossRef](#)]
21. Kadri, Y.; Hadj Abdallah, H. Performance evaluation of a stand-alone solar dish Stirling system for power generation suitable for off-grid rural electrification. *Energy Convers. Manag.* **2016**, *129*, 140–156. [[CrossRef](#)]
22. Meinhardt, M.; Cramer, G.; Burger, B.; Zacharias, P. Multi-string-converter with reduced specific costs and enhanced functionality. *Sol. Energy* **2001**, *69*, 217–227. [[CrossRef](#)]
23. Wu, B.; Lang, Y.; Zargari, N.; Kouro, S. *Power Conversion and Control of Wind Energy Systems*; Wiley: Hoboken, NJ, USA, 2011.
24. Li, Y.; Choi, S.S.; Yang, C. An average-value model of kinematic Stirling engine for the study of variable-speed operations of dish-stirling solar-thermal generating system. In Proceedings of the 11th IEEE International Conference on Control and Automation (ICCA), Taichung, Taiwan, 18–20 June 2014; pp. 1310–1315.
25. Trifkovic, M.; Sheikhzadeh, M.; Nigim, K.; Daoutidis, P. Modeling and Control of a Renewable Hybrid Energy System With Hydrogen Storage. *IEEE Trans. Control Syst. Technol.* **2014**, *22*, 169–179. [[CrossRef](#)]
26. Kundur, P.; Balu, N.J.; Lauby, M.G. *Power System Stability and Control*; McGraw-Hill: New York, NY, USA, 1994.
27. Arnalte, S.; Burgos, J.C.; Rodríguez-Amenedo, J.L. Direct Torque Control of a Doubly-Fed Induction Generator for Variable Speed Wind Turbines. *Electr. Power Compon. Syst.* **2002**, *30*, 199–216. [[CrossRef](#)]
28. Poli, R.; Kennedy, J.; Blackwell, T. Particle swarm optimization. *Swarm Intell.* **2007**, *1*, 33–57. [[CrossRef](#)]
29. Venter, G.; Sobieszczanski-Sobieski, J. Particle Swarm Optimization. *AIAA J.* **2003**, *41*, 1583–1589. [[CrossRef](#)]



© 2019 by the authors. Licensee MDPI, Basel, Switzerland. This article is an open access article distributed under the terms and conditions of the Creative Commons Attribution (CC BY) license (<http://creativecommons.org/licenses/by/4.0/>).